Exploration of Neuroscience

Open Exploration

Open Access Original Article

MK-801-induced cognitive dysfunction in a schizophrenia model: mechanistic links between interstitial fluid drainage impairment and neural metabolic disturbances

Xin Mao[1,2,3], Tianzi Gao[3,4], Shufan Yang[5], Hanbo Tan[3,4], Shaoyi Su[3,6,7*], Ren Long[8*]

[1]Department of Radiology, Aerospace Center Hospital, Peking University Aerospace School of Clinical Medicine, Beijing 100049, China

[2]Department of Radiology, Peking University Third Hospital, Beijing 100191, China

[3]Beijing Key Laboratory of Intelligent Neuromodulation and Brain Disorder Treatment, Peking University Third Hospital, Beijing 100191, China

[4]Institute of Medical Technology, Peking University Health Science Center, Beijing 100191, China

[5]Department of Neurosurgery, The Second Qilu Hospital of Shandong University, Jinan 250013, Shandong, China

[6]Aerospace Medical Center, Aerospace Center Hospital, Peking University Aerospace School of Clinical Medicine, Beijing 100049, China

[7]GENERTEC Key Laboratory of Aerospace Medical Research and Transformation, Beijing 100049, China

[8]School of Public Health, Peking University Health Science Center, Beijing 100191, China

***Correspondence:** Shaoyi Su, Aerospace Medical Center, Aerospace Center Hospital, Peking University Aerospace School of Clinical Medicine, Beijing 100049, China. sushaoyi@bjmu.edu.cn; Ren Long, School of Public Health, Peking University Health Science Center, Beijing 100191, China. 2411110232@stu.pku.edu.cn

Academic Editor: Aurel Popa-Wagner, University of Medicine and Pharmacy Craiova, Romania

Received: January 17, 2026 **Accepted:** April 23, 2026 **Published:** July 2, 2026

Cite this article: Mao X, Gao T, Yang S, Tan H, Su S, Long R. MK-801-induced cognitive dysfunction in a schizophrenia model: mechanistic links between interstitial fluid drainage impairment and neural metabolic disturbances. Explor Neurosci. 2026;5:1006140. https://doi.org/10.37349/en.2026.1006140

Abstract

Aim: To investigate the mechanisms underlying MK-801-induced schizophrenia-like cognitive dysfunction by examining the interplay between brain interstitial fluid (ISF) drainage impairment, myelin structural integrity, and regional neurometabolic disturbances.

Methods: Mice received chronic administration of MK-801 (2 mg/kg/day) for two weeks to induce schizophrenia-like phenotypes. Cognitive function and sensorimotor gating were evaluated using the novel object recognition test and pre-pulse inhibition (PPI) assessment. ISF drainage patterns were visualized via fluorescent tracing with Lucifer Yellow. Myelin integrity in the internal capsule was quantified using Luxol Fast Blue (LFB) staining and transmission electron microscopy (TEM). Regional metabolic profiles in the caudate nucleus and thalamus were analyzed using untargeted metabolomics.

Results: MK-801 treatment resulted in significant recognition memory impairment and sensorimotor gating deficits. Fluorescent tracing revealed pathological ISF reflux from the caudate nucleus toward the thalamus, which was restricted in control mice. This drainage failure corresponded to severe demyelination and ultrastructural damage in the internal capsule, characterized by increased myelin thickness and a significantly decreased G-ratio. Furthermore, regional metabolomic analysis identified distinct dysregulation of tryptophan metabolism in the caudate nucleus and tyrosine metabolism in the thalamus.

Conclusions: Myelin degradation in the internal capsule disrupts the structural barrier required for compartmentalized ISF drainage. The resulting ISF reflux facilitates regional metabolic imbalances, particularly within tryptophan and tyrosine pathways, suggesting that fluidic dynamics failure is a critical contributor to the neurochemical pathology of schizophrenia.

Keywords

MK-801, cognition, neurometabolite, interstitial fluid

Introduction

MK-801, an *N*-methyl-*D*-aspartate (NMDA) receptor antagonist, can induce schizophrenia (SZ)-like behaviors in mice and is widely used as a pharmacological model for SZ [1]. SZ is a group of syndromes characterized by unclear etiology, with clinical manifestations including hallucinations, thought disorders, hyperkinesia, anxiety, and cognitive impairment [2]. Patients with this disease exhibit significant heterogeneity in clinical features, treatment responses, and long-term prognosis. Long-term illness not only imposes dual health and economic pressures on patients and their families but also causes a heavy socioeconomic burden [3]. In recent years, the global disease burden of SZ has been increasing annually. A statistical study showed that the prevalence of SZ increased from 14.2 million in 1990 to 23.6 million in 2019, with a relative increase of 65%; the incidence rate rose from 941,000 to 1.3 million, a relative increase of 37%; and the disability-adjusted life years (DALYs) increased from 9.1 million to 15.1 million, also a relative increase of 65% [4]. Meanwhile, a study on economic burden indicated that the estimated economic burden of SZ in the United States in 2019 was $343.2 billion, more than twice the estimated value in 2013 [5].

Despite the severe harm of SZ to individuals and society, there is still no unified conclusion in the academic community regarding its pathogenesis [6, 7]. The neurochemical pathology hypothesis is a widely accepted etiological hypothesis for SZ, which holds that schizophrenic patients have intracerebral metabolic disorders, leading to imbalances of certain chemical substances in the brain. This is mainly manifested by abnormal accumulation or excessive consumption of neurotransmitters, thereby interfering with normal intracerebral signal transmission and nerve impulse conduction [8, 9]. A growing body of evidence suggests that the core pathophysiological changes of SZ may involve functional disorders of dopaminergic, glutamatergic, serotonergic, and γ-aminobutyric acid (GABA) signaling pathways, rather than being caused by abnormalities in a single signaling pathway [10, 11].

The transmission of neurotransmitters between neurons depends on interstitial fluid (ISF) in the brain, which is widely distributed in the extracellular space. Recent studies have found that the normal drainage of ISF relies on the densely arranged myelin sheaths in the brain, which can limit the drainage direction of ISF and form a barrier for the zonal drainage of ISF [12, 13]. In addition, myelin development is closely related to the formation of cognitive functions. Multiple clinical experimental evidences have shown that patients with SZ have extensive abnormal myelination of white matter tracts in the brain [14, 15]. Based on this, specific myelin damage is considered to be able to cause secondary abnormal zonal drainage of ISF, further aggravating the imbalance of neurometabolic substances in the brain. Previous studies related to SZ have mostly focused on genetic factors, neuronal development, and signal transduction pathways, while studies on the role of myelin and ISF drainage changes in SZ and the relationship between them are still scarce in the academic community [16, 17].

Based on the above research background, this study aims to explore the drainage characteristics of brain ISF and its secondary neurometabolic abnormalities behind MK-801-induced cognitive dysfunction.

Materials and methods

Experimental animals

All animal surgical procedures and usage protocols in this study were strictly conducted in accordance with the Guidelines of the Chinese Animal Welfare and Ethics Committee (GB/T3589-2018), and the experiment was approved by the Biomedical Ethics Committee of Peking University (approval number: LA2022325). The experimental animals were purchased from Beijing Vital River Laboratory Animal Technology Co., Ltd. SPF-grade female C57BL/6J mice (6–8 weeks old, weighing 20 ± 2 g) were randomly divided into 2 groups: the model group and control group. The mice were housed under controlled laboratory conditions (room temperature: 20 ± 1°C; light/dark cycle: 12 h) with free access to food and water. All behavioral tests were performed during the light phase.

To further ensure compliance with animal welfare and ethical guidelines, predefined humane endpoints were implemented throughout the experiment: these criteria included body weight loss of 20% or more relative to the baseline body weight, inability to independently access food or water for more than 24 consecutive hours, severe motor dysfunction such as persistent paralysis or convulsive seizures, and abnormal respiratory patterns like rapid shallow breathing or pre-asphyxial signs; the body weight, behavioral status, and physiological performance of the mice were monitored daily, and any mouse meeting any of these criteria was immediately euthanized via an overdose of sodium pentobarbital (240 mg/kg) followed by cervical dislocation to minimize animal suffering.

Animal modeling

Mice were randomly divided into two groups to explore the pathological changes of MK-801-induced cognitive dysfunction in SZ mice, and the scheme diagram is shown in Figure 1. The mice in the model group received continuous intraperitoneal injection (i.p.) of MK-801 (Sigma-Aldrich Corporation) for two weeks, with a dose of 2 mg/kg/day; while the mice in the control group received continuous i.p. of saline for two weeks, with a dose of 2 mg/kg/day [18].

Novel object recognition

One day after the completion of the open-field test, a novel object recognition experiment was conducted (provided by the Beijing Key Laboratory of Magnetic Resonance Imaging and Technology). The experimental box for the mice had a size of 50 cm × 50 cm × 40 cm. During the familiarization phase, two identical wooden objects were placed in the center of the experimental box, equidistant from the walls. The mice were allowed to freely explore the box for ten minutes. In the testing phase on the following day, one of the objects in the experimental box was replaced with a different shape, and the mice were allowed to freely explore for ten minutes. The mice's exploration behavior towards the novel and familiar objects was recorded using a camera installed on the top of the experimental box, and the recognition index (RI) was analyzed using computer-based animal behavior analysis software (provided by Beijing Zhong Shi Di Chuang Technology Development Co., Ltd.). The formula for calculating the RI was RI = TN / (TN + TF), where TN represents the time spent exploring the novel object, and TF represents the time spent exploring the familiar object. After each trial, the experimental box was cleaned with a 45% ethanol solution [19].

Pre-pulse inhibition (PPI)

After the novel object recognition evaluation, a PPI experiment was carried out to assess the sensorimotor gating (SG) of the mice, whose functional damage is manifested in the attention deficit and thought disorders of schizophrenic patients. The Xeye Startle system (provided by Beijing Zhong Shi Di Chuang Technology Development Co., Ltd.) was used in the experiment. One day before the test, the mice were placed in the behavioral testing laboratory to adapt to the environment. Prior to the experiment, the background noise of the experimental box was set to 70 dB, and the startling pulse was set to 120 dB. The pre-pulse intensity was set to 3 dB above the background noise level (PPI3), 6 dB above the background noise level (PPI6), and 12 dB above the background noise level (PPI12). The single experiment was divided into four stages (Blocks 1–4), each appearing sequentially. Blocks 1 and 4 consisted of 6 individual startling

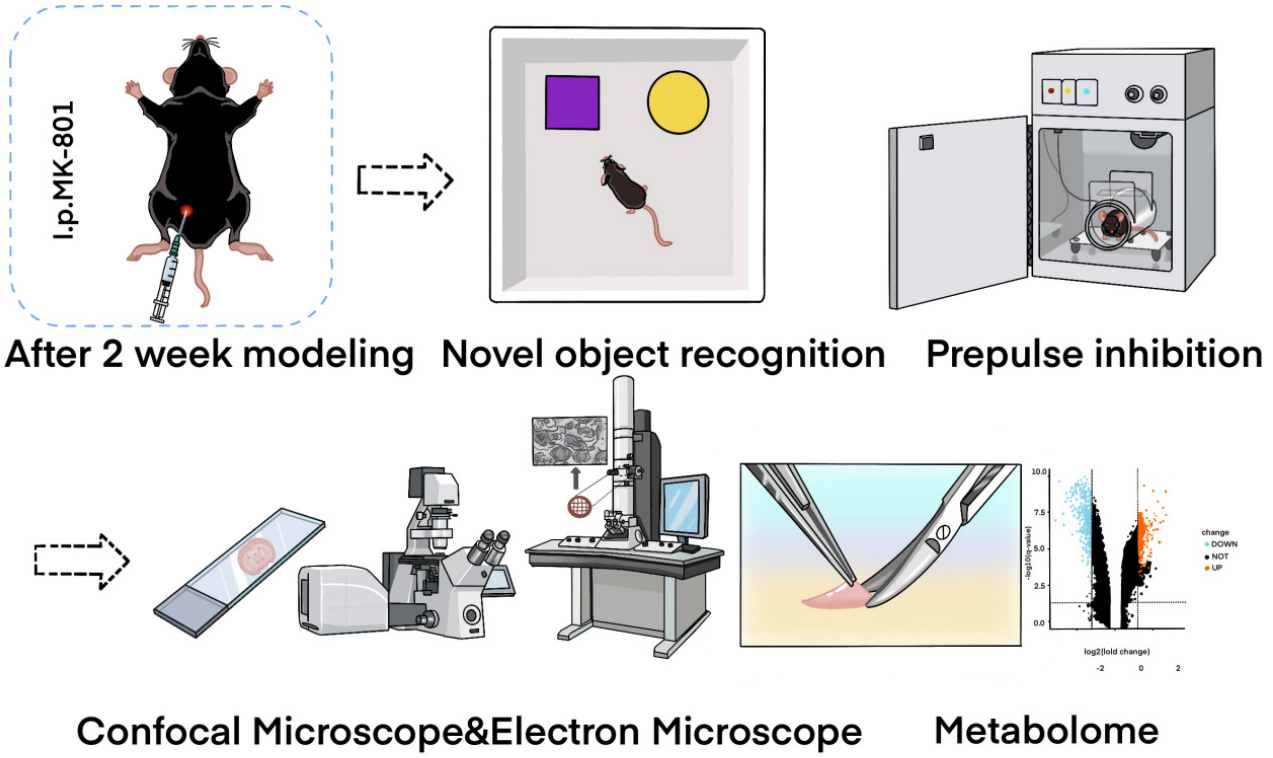

Figure 1. Schematic diagram of the core mechanism exploration in this study. This figure illustrates the potential pathway by which MK-801 induces schizophrenia-like cognitive dysfunction. With 2 weeks: After a 2-week MK-801 intervention, cognition was evaluated via behavior tests, and then, the brain interstitial fluid (ISF) and pathological changes were detected. Consequently, this leads to the imbalance of neurometabolic substances, which were examined as well. i.p.: intraperitoneal injection.

pulses. Blocks 2 and 3 consisted of 6 separate startling pulses, 5 PPI3+startling pulse stimulus patterns, 5 PPI6+startling pulse stimulus patterns, 5 PPI12+startling pulse stimulus patterns, and 5 white noise stimulus patterns with no startling pulse stimulus. The pre-pulse duration was 20 ms, and the startling pulse duration was 40 ms, with a time interval of 100 ms (from start to start) between the pre-pulse and the startling pulse. Each stimulus mode appeared randomly, and the time interval between each mode was randomly set between 5 and 23 s. At the beginning of the experiment, the mice were fixed in a transparent glass box and allowed to adapt to the background noise for 5 minutes before sequentially undergoing the four experimental stages. The recorded peak amplitude (mv) was used to determine the amplitude of the startle response, where the average response amplitude in trials with only startling pulses (S) and in trials with both pre-pulse and startling pulses (PPI_S) was calculated. The formula for calculating the PPI rate (i.e., PPI%) of the startle response amplitude was PPI% = 100 × (S – PPI_S) / S [20].

Fluorescence tracing

Mice were anesthetized with 3% isoflurane for induction and 1–2% isoflurane for maintenance via inhalation during surgical procedures, with continuous monitoring of respiratory rate and reflexes. The scalp was incised with a razor blade to expose the skull, and the bregma was marked. The head was horizontally fixed to a stereotaxic instrument, with the bregma as the origin. According to the stereotaxic atlas of the mouse brain, the location of the caudate nucleus was identified and marked (0.7 mm anterior, 1.7 mm right, and 3 mm deep). Using a skull drill, the corresponding position on the skull was drilled, and a fine glass capillary needle was used to draw 10 mmol/L Lucifer Yellow solution and fixed to a microinjection pump. The infusion volume was set at 1 μL, with an injection speed of 0.2 μL/min. The solution was then injected into the corresponding brain region using the microinjection pump. After the

completion of the injection, the needle was kept in place for 10 min before slowly withdrawing to avoid liquid reflux. After diffusion for 1 hour, brain perfusion was performed, and the mouse brain was removed and fixed overnight in 4% paraformaldehyde at 4°C. The next day, the mouse brain was removed and sectioned into slanting sagittal sections: the brain was placed in a slicing mold, and a slanted sagittal position was made at a 15° angle along the direction connecting the thalamus and caudate nucleus, with a thickness of 1 mm. The observation surface was placed on a confocal dish for imaging using a confocal laser scanning microscope (CLSM) and was primarily observed with a stereoscope. For fluorescence imaging, the imaging settings for CLSM were as follows: Lucifer Yellow excitation light at 488 nm and emission light at 510–550 nm; myelin sheath reflection excitation light at 633 nm and emission light at 630–640 nm. The panorama function of the Leica DIVE confocal microscope was used to store m × n images during the scanning process, and the LSCM Merging function was used to reconstruct the fluorescence images to obtain a complete image of the specified region of the sample [21].

Untargeted metabolomics

After the behavioral experiments, mice were decapitated, and their brains were placed in PBS buffer. Under a small animal surgical microscope, the caudate nucleus and thalamus tissues were rapidly dissected using surgical blades and forceps and stored in liquid nitrogen for further experiments. High-resolution mass spectrometry data were collected using the Q Exactive mass spectrometer (Thermo Fisher Scientific, USA) in both positive and negative ion modes to improve metabolite coverage. Data processing was performed using Compound Discoverer 3.0 software (Thermo Fisher Scientific, USA), and metabolite identification was based on the mzCloud (Thermo Fisher Scientific, USA) and BGI library databases (BGI Genomics, Shenzhen, China). Differential metabolites between the model group, treatment group, and control group were screened using the R software package metaX. Preprocessing steps included: 1) Normalization of data to obtain relative peak areas by Probabilistic Quotient Normalization (PQN); 2) Correction of batch effects using quality control (QC)-based robust LOESS signal correction; 3) Removal of metabolites with a coefficient of variation greater than 30% in QC samples. A principal component analysis (PCA) plot was generated to reflect the distribution of QC samples, assessing instrument stability and data reproducibility. For discriminant analysis, partial least squares-discriminant analysis (PLS-DA) was employed to screen for differences between groups, utilizing PLS regression to model the relationship between metabolite expression and sample categories. Metabolic pathway enrichment analysis of differential metabolites based on the KEGG database was analyzed as well [22].

Luxol Fast Blue (LFB) staining

LFB myelin staining was used to investigate the demyelination in the mouse brain. After behavioral experiments, the mice were perfused, and the brains were fixed in 4% paraformaldehyde at 4°C for 24 hours. Subsequently, the brains were dehydrated in gradient sucrose solutions with concentrations of 15%, 20%, and 30% overnight, embedded in freezing embedding medium, and sectioned using a cryostat microtome. The oblique sagittal sections were obtained by rotating 15° outward from the midline of the cerebellum. The sections had a thickness of 20 μm and were mounted on slides, then incubated at 37°C for 12 hours. After sectioning, the brain slices were stored at –20°C.

Before staining, the embedding medium surrounding the tissue was washed away with distilled water. The tissue was hydrated in 95% ethanol, rinsed with distilled water, and stained with 0.1% LFB staining solution at room temperature. Excess stain was removed by rinsing the slides in 95% ethanol, followed by a rinse with distilled water. The differentiation solution, composed of 0.05% lithium carbonate and 70% ethanol, was used for differentiation until the gray and white matter were clearly distinguished. After rinsing with distilled water, the slides were mounted. Images were acquired by optical microscopy and analyzed with CAM-MS software (V3.1, CNC Software Inc.). Myelin sheaths appeared blue, while other structures remained mostly unstained. The internal capsule area was analyzed by a blinded observer, and the mean optical density (OD) value of the internal capsule was analyzed as well [23].

Electron microscopy

The mice were decapitated, and the brains were placed in PBS buffer. Under a surgical microscope, the internal capsule region connecting the caudate nucleus and thalamus was quickly dissected using a scalpel and forceps. Tissue samples of approximately 1 mm^3 in size were collected and placed in a fixative solution specifically for electron microscopy, and tissues were fixed in 2.5% glutaraldehyde in 0.1 M phosphate buffer (pH 7.4) for 24 h at 4°C. On the following day, the tissue was fixed with 1% osmium tetroxide at room temperature for 2 hours in a darkroom. The tissue was dehydrated using a series of graded alcohols: 30%, 50%, 70%, 80%, 90%, and two rounds of 100%, with each step lasting 20 min. Then, the tissue was dehydrated twice with 100% acetone for 15 min each time. The tissue was embedded in epoxy resin to prepare resin blocks. Ultrathin sections (80 nm thick) were cut using an ultramicrotome and collected on 150-mesh copper grids with a carbon support film. The copper grids with tissue sections were stained with 2% uranyl acetate saturated in ethanol for 8 min in a darkroom. After staining, the grids were washed three times with 70% ethanol and then rinsed three times with ultrapure water. The sections were further stained with 2.6% lead citrate solution for 8 min, followed by three washes with ultrapure water. Excess water was removed using filter paper, and the copper grids with tissue sections were placed in a copper grid box to air dry overnight. Then, ultrathin sections were collected on copper grids, and the ultrastructural alterations of the myelin sheath were detected by transmission electron microscopy (TEM, HT7700, Hitachi). The thickness of the myelin sheath and myelinated axon was measured. Besides, the inner and outer diameters of myelinated axons quantified by ImageJ were used as the parameters to calculate area and number of myelinated axons (Quantity ratio), G-ratio, and myelin sheath thickness [24].

Statistics

The experimental data were statistically analyzed using R software. GraphPad Prism version 9.5 for Windows was used to create statistical charts. The experimental results were presented as mean ± standard deviation. Data normality was assessed using Shapiro-Wilk tests, and for data that followed a normal distribution, a *t*-test was used to analyze the differences among the groups. For non-normally distributed data, the Mann-Whitney *U* test was used to compare the differences among the groups. A significance level of $P < 0.05$ was considered statistically significant for intergroup differences.

Results

Systemic functional changes and cognitive dysfunction in SZ mice

To evaluate the cognitive function and SG ability of the MK-801-induced SZ model mice, novel object recognition test and PPI test were performed, and the related behavioral indicators were statistically analyzed. The novel object recognition test is a classic method to assess the recognition memory function of rodents, and the movement trajectory, cognitive index, and exploration times of novel objects can comprehensively reflect the cognitive status of mice.

As shown in Figure 2A, the movement trajectory of SZ model mice in the novel object recognition test was relatively scattered, with no obvious preference for the novel object area; while the Sham group mice showed a concentrated trajectory, and spent more time exploring the novel object area. Quantitative analysis showed that the cognitive index of the SZ model mice was significantly lower than that of the Sham group ($P < 0.01$, Figure 2B), indicating that the SZ model mice had obvious recognition memory impairment, which was consistent with the core cognitive dysfunction phenotype of SZ. In terms of the number of explorations of novel objects, the SZ model group showed a significant decrease compared with the control group ($P < 0.01$, Figure 2C). The reduction in the number of explorations of novel objects reflects the decrease in the exploration willingness of SZ mice to novel stimuli, which is closely related to the negative symptoms, such as apathy in SZ.

The PPI test is an important method to evaluate the SG function of the brain, and the impairment of PPI is one of the typical neurobehavioral characteristics of SZ. To exclude the interference of basic auditory function on the test results, the auditory response of mice without stimulation was first detected. The

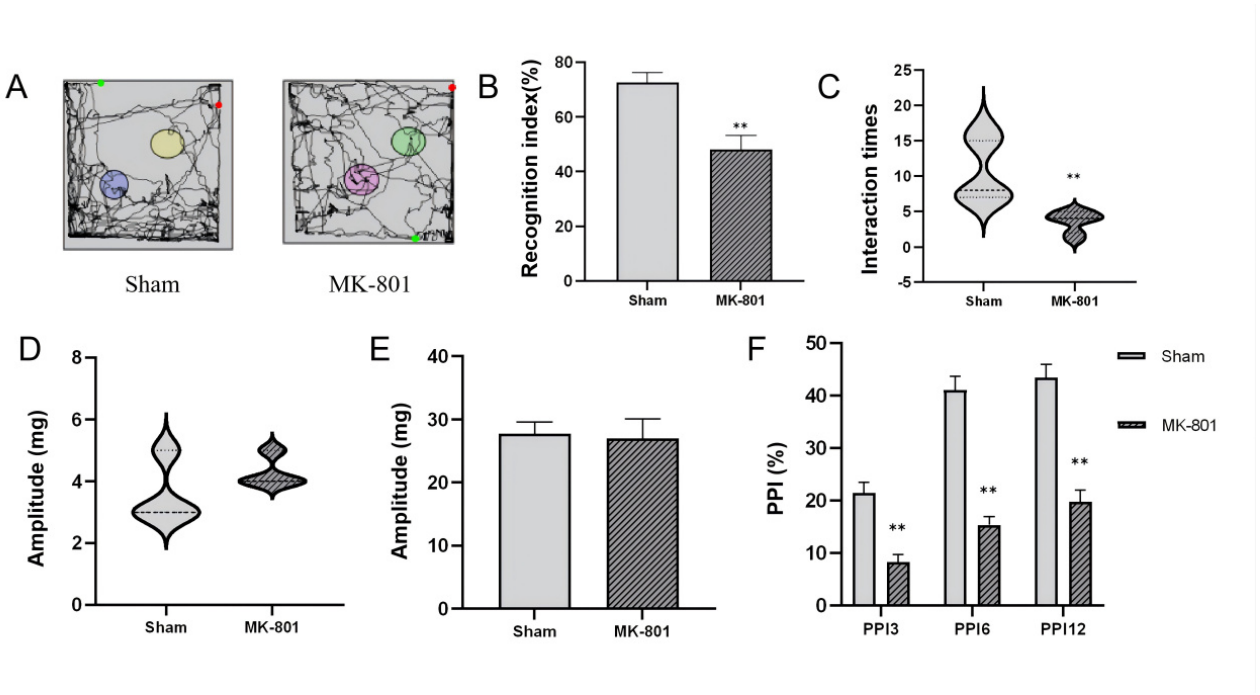

Figure 2. Behavioral test results of mice. (**A**) Movement trajectories of mice in the novel object recognition test, reflecting the activity range and exploration preference of mice in the experimental area; (**B**) Statistical comparison of cognitive index between the two groups, which is a core indicator for evaluating the recognition memory ability of mice to novel objects; (**C**) Statistical analysis of the number of explorations to novel objects in the two groups; (**D**) Auditory response intensity of mice without stimulation in the pre-pulse inhibition (PPI) behavioral test; (**E**) Statistical analysis of auditory response intensity to startle stimulation in the two groups; (**F**) Statistical comparison of PPI rate of startle reflex between the two groups. Data are presented as mean ± standard error, with error bars representing standard error. Compared with the Sham group, $^{**}P < 0.01$, indicating statistically significant differences. $n = 7$ per group.

results showed that there was no significant difference in the auditory response intensity between the SZ model group and the Sham group under the condition of no stimulation ($P > 0.05$, Figure 2D), indicating that the basic auditory function of SZ model mice was not affected, and the subsequent PPI index changes were not caused by auditory dysfunction. Similarly, when stimulated by startle stimuli, the response intensity did not reveal a significant difference ($P > 0.05$, Figure 2E). The PPI rate of startle reflex, the core index of the PPI test, was significantly reduced in the SZ model group compared with the Sham group (all $P < 0.01$, Figure 2F). The decrease in PPI rate indicates that the SG function of SZ model mice is damaged, and the brain cannot effectively filter irrelevant sensory information, which is consistent with the information processing disorder of SZ patients. In summary, the SZ model mice induced by MK-801 showed significant cognitive dysfunction and SG impairment, which fully reproduced the core behavioral phenotypes of SZ, providing a reliable behavioral basis for subsequent studies on the pathological mechanism of SZ.

Reflux of ISF in the brain regions of SZ mice affects the caudate nucleus and thalamus

Based on the compartmentalized ISF drainage pathway, we further detected the ISF reflux level in SZ model mice to clarify its distribution characteristics in multiple brain regions and correlation with behavioral phenotypes. The ISF drainage function is closely related to the clearance of neurometabolic wastes, and it is expected to be a key link connecting the pathophysiological mechanism.

To investigate changes in regional ISF drainage between brain regions, a stereotactic injector was used to inject the fluorescent tracer Lucifer Yellow into the caudate nucleus to explore ISF drainage changes. Figure 3A shows the comparison of the fluorescence diffusion area towards the posterior thalamus between the model group and the control group after 1 hour of tracer diffusion. Figure 3B shows the tracer diffusion situation captured by the camera under oblique sagittal sections. In the model group, the tracer crossed the barrier structure and refluxed into the posterior thalamus area, whereas in the control group, the tracer from the caudate nucleus did not reflux into the posterior thalamus area. The model group exhibited significantly larger diffusion area in the thalamus region ($P < 0.01$, Figures 3C–D), compared to

the control group. This suggests that the model group of mice experienced disruption in ISF drainage between the caudate nucleus and the thalamus. In conclusion, the SZ model mice induced by MK-801 have significant ISF reflux abnormality in multiple core brain regions, and this abnormality is closely correlated with the core behavioral phenotypes of SZ.

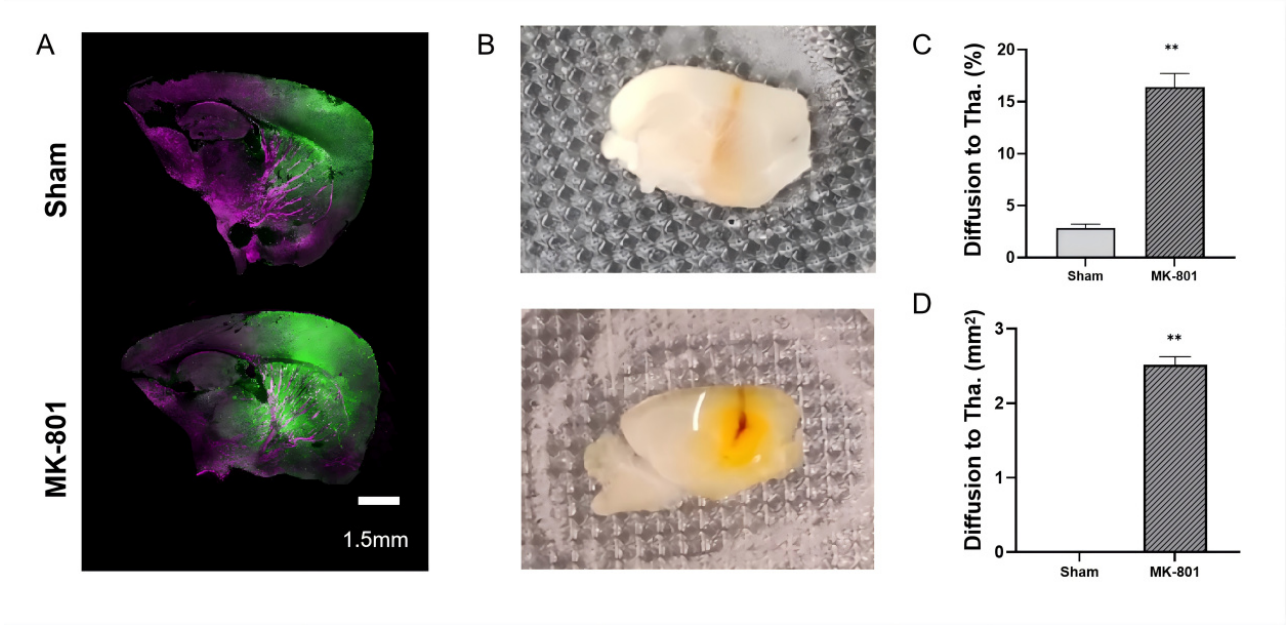

Figure 3. Brain interstitial fluid (ISF) reflux level in SZ model mice (*n* = 4 per group). (**A**) Extracellular fluorescent tracer reflux level from the caudate nucleus towards the posterior thalamus; (**B**) ISF reflux situation under observation with a stereomicroscope; (**C**) Proportion of abnormal diffusion area; (**D**) Diffusion area to thalamus. Data are presented as mean ± standard error, with error bars representing standard error. Compared with the Sham and MK-801 groups, $^{**}P < 0.01$; Tha.: thalamus.

Regional-specific metabolic pathway dysregulation in caudate nucleus and thalamus of SZ mice

Small-molecule neurometabolic substances reside in ISF, closely linked to cellular metabolism, secretory processes, and extracellular information transfer. Therefore, ISF drainage maintains the bridge of the metabolic connectome [25]. Consequently, we first investigated the effect of ISF decompartmentalization on region-specific neuro-metabolism within the thalamus and caudate nucleus ISF, under the scenario of spontaneous ISF reflux in SZ mice. To further elucidate the impact of MK-801-induced ISF drainage disruption on neuro-metabolic substance distribution, we analyzed metabolic profiles via global analysis (Figure 4A). Metabolite classification showed lipids and compounds with biological roles, such as amino acids, alcohols, imidazole, phenols and derivatives, pyridine and derivatives, engaging in amino acid metabolism, lipid, nucleotide, and carbohydrate metabolism.

PLS-DA (Figure 4B) demonstrates that the sham group shows a clearer separation trend, underscoring significant differences in metabolic profiles. The volcano plots (Figure 4C, Table S1) identify numerous differentially expressed metabolites, highlighting the altered metabolic landscape in MK-801-treated mice. The heatmap (Figure 4D) displays distinct metabolite expression patterns, further confirming that MK-801-induced ISF drainage disorder disrupts the distribution of neuro-metabolic substances. Collectively, these results show that MK-801-mediated ISF drainage dysfunction leads to profound disturbances in neuro-metabolic substance distribution, impacting multiple metabolic profiles.

To clarify the metabolic regulatory networks underlying ISF reflux-induced brain region dysfunction, we performed KEGG pathway enrichment analysis on differential metabolites between MK-801 and Sham groups in the caudate nucleus and thalamus (Figure 4E), aiming to identify pathway-level metabolic abnormalities associated with SZ. For the caudate nucleus (left panel of Figure 4E), multiple pathways were significantly enriched ($P < 0.05$) among differential metabolites: Pathways included tryptophan

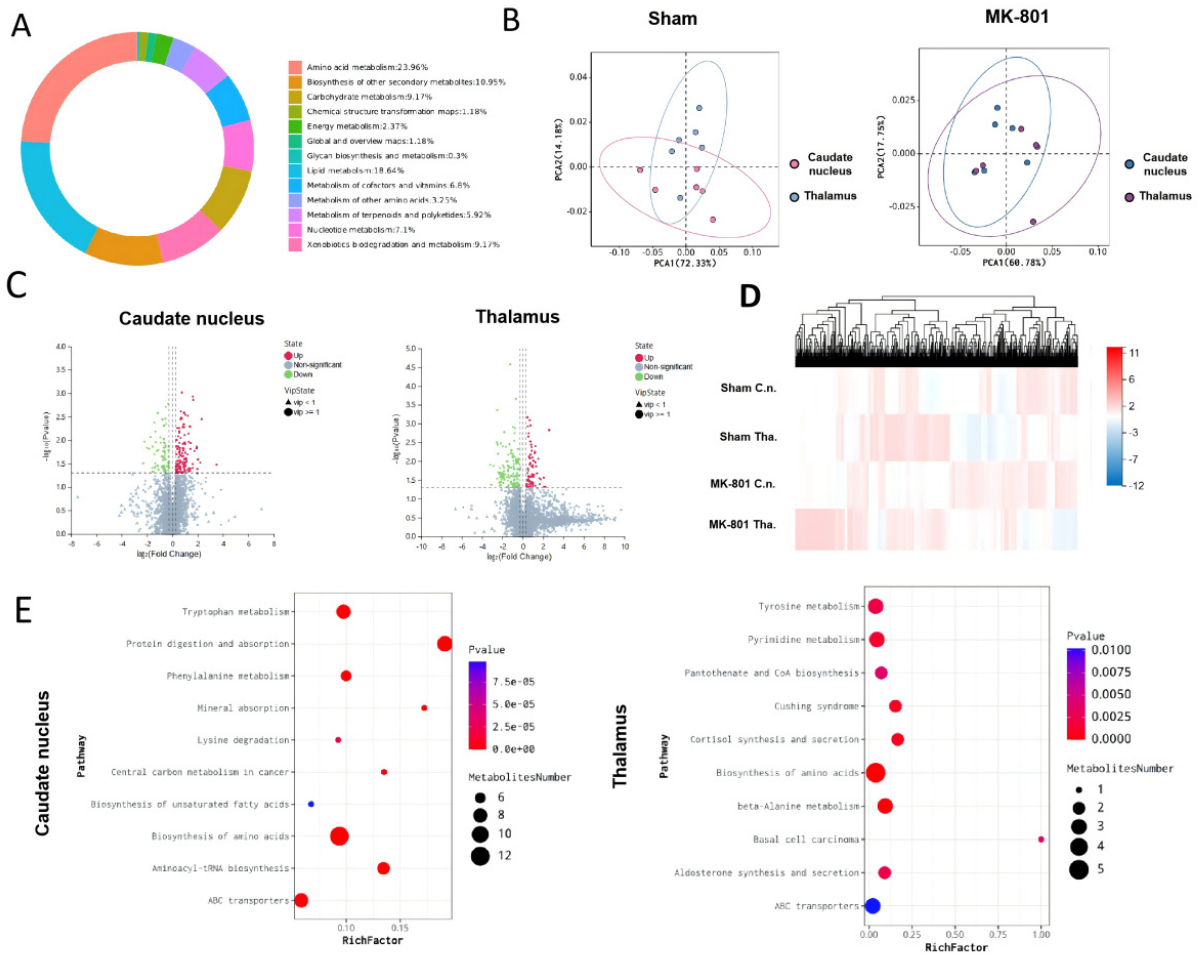

Figure 4. Effects of MK-801-induced interstitial fluid (ISF) drainage disruption on neuro-metabolite distribution and metabolic pathway enrichment analysis in SZ model mice. (**A**) Pie chart of metabolite classification: showing the proportion of different differential metabolite categories; (**B**) Partial least squares-discriminant analysis (PLS-DA) plots: presenting the metabolic profile distribution of Sham (left) and MK-801 (right) groups; (**C**) Volcano plots: displaying differential metabolites in the caudate nucleus (left) and thalamus (right), where $\log_2$(Change) represents the relative fold change of metabolites, and $-\log_{10}$(P) represents the significance of differences; red dots indicate upregulated differential metabolites, green dots indicate downregulated differential metabolites, and gray dots indicate non-significant metabolites; (**D**) Metabolite expression heatmap: the color gradient (from red to blue) represents the relative expression level of metabolites (red = high expression, blue = low expression); (**E**) Bubble plots of KEGG pathway enrichment: showing pathway enrichment results of differential metabolites in the caudate nucleus (left) and thalamus (right), where the color gradient corresponds to *P*-value (n = 6 per group). C.n.: caudate nucleus; Tha.: thalamus.

metabolism, protein digestion and absorption, and biosynthesis of amino acids. For the thalamus (right panel of Figure 4E), the enriched pathways differed from those in the caudate nucleus, reflecting region-specific metabolic dysregulation, and the most significantly enriched pathways ($P < 0.01$) included tyrosine metabolism, pyrimidine metabolism, and biosynthesis of amino acids. In summary, the caudate nucleus and thalamus of MK-801-induced SZ mice exhibit distinct, region-specific metabolic pathway dysregulation, and this regional specificity of metabolic dysfunction may give rise to the functional characteristics of each brain region, further linking ISF reflux-induced metabolic disorders to the core behavioral phenotypes of SZ.

Impaired ISF drainage barrier between the caudate nucleus and thalamus of SZ mice

The internal capsule—a bundle of dense myelinated fibers between the thalamus and caudate nucleus—serves as a critical structural barrier that restricts directional ISF drainage between these two brain regions. To assess the integrity of this barrier in SZ mice, we performed LFB myelin staining targeting the internal capsule. Morphological observations revealed overt disruption of myelin integrity in the internal capsule area of MK-801-treated mice, accompanied by reduced myelin sheath density (Figure 5A). Quantitative analyses further confirmed these structural abnormalities: the proportion of myelin structure

area in the MK-801 group was significantly lower than that in the Sham group ($P < 0.01$; Figure 5B). Correspondingly, the mean OD in the MK-801 group was also markedly decreased compared to the Sham group ($P < 0.01$; Figure 5C). These data collectively indicate severe myelin loss in the internal capsule of SZ mice, which compromises the structural basis of the ISF drainage barrier.

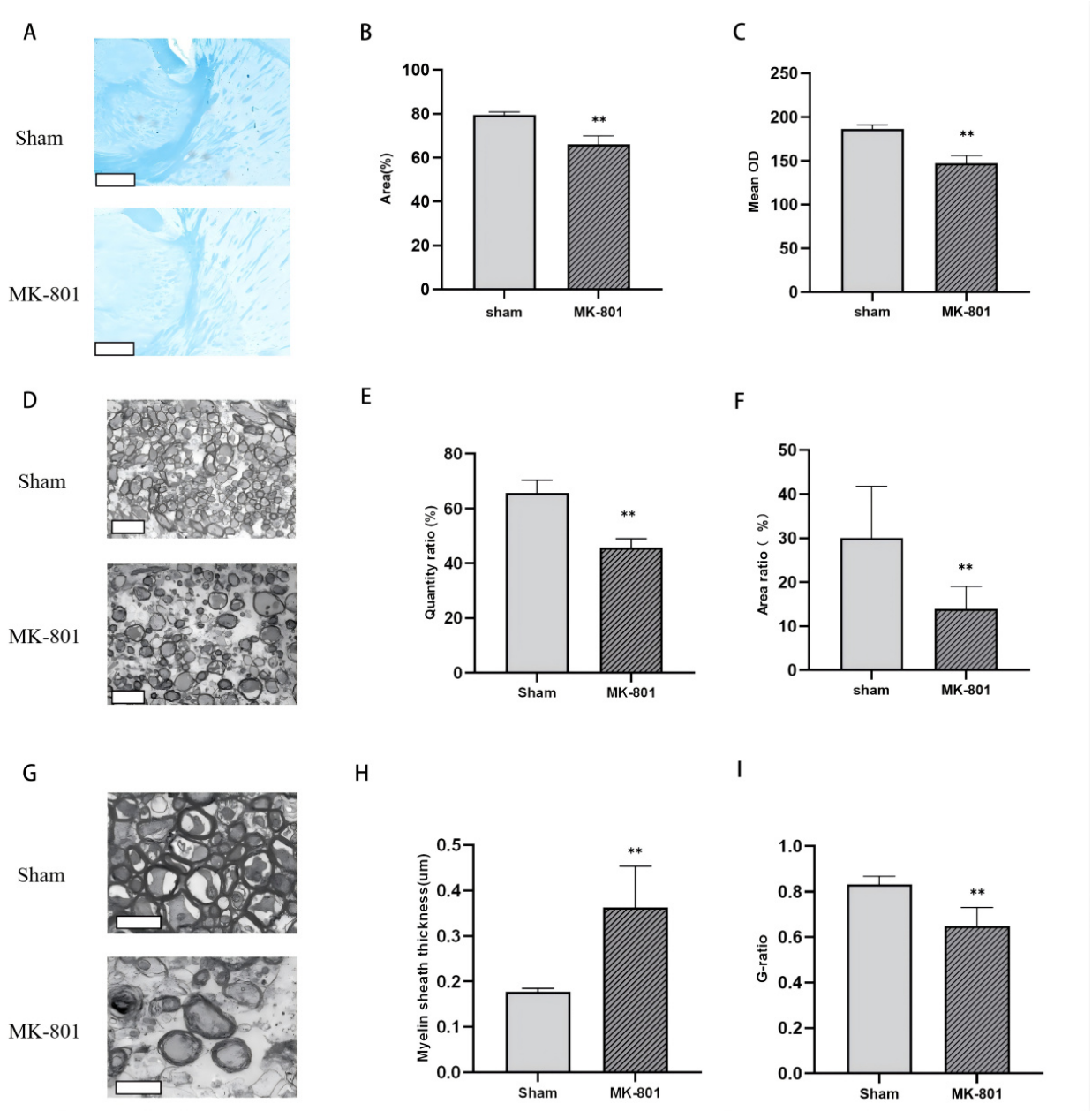

Figure 5. Impairment of the interstitial fluid (ISF) drainage barrier between the caudate nucleus and thalamus, and brain region-specific ISF reflux analysis in SZ model mice. (**A**) Luxol Fast Blue (LFB) myelin staining of the internal capsule, scale bar = 400 μm; (**B**) Statistical analysis of the myelin structure area proportion in the internal capsule; (**C**) Statistical analysis of the mean optical density (OD) of myelin in the internal capsule; (**D**) Low-magnification transmission electron microscopy (TEM) images of the internal capsules, scale bar = 5 μm; (**E**) Statistical analysis of the quantity ratio of myelinated fiber bundle; (**F**) Statistical analysis of the area ratio of myelinated fiber bundles; (**G**) High-magnification TEM images of the internal capsule scale bar = 2 μm; (**H**) Statistical analysis of myelin sheath thickness; (**I**) Statistical analysis of myelin G-ratio. Compared with the Sham group, $^{**}P < 0.01$; ($n = 4$ per group).

To characterize myelin pathology at the ultrastructural level, we used TEM to examine the internal capsule. Low-magnification TEM images showed that the density and structural integrity of myelin bundles in the internal capsule were substantially disrupted in the MK-801 group (Figure 5D). Quantitative TEM analyses demonstrated that both the quantity ratio ($P < 0.01$; Figure 5E) and area ratio ($P < 0.01$; Figure 5F) of myelinated fiber bundles in the model group were significantly reduced relative to the control group.

High-magnification TEM further revealed prominent demyelination in the dense myelin sheath structure of the internal capsule in MK-801-treated mice (Figure 5G). Consistent with structural damage, the myelin sheath thickness in the model group was significantly increased (P <0.01; Figure 5H), while the G-ratio (the ratio of axon diameter to total fiber diameter, an indicator of myelin compaction) was significantly decreased (P <0.01; Figure 5I) compared to the Sham group. These ultrastructural findings align with LFB staining results, confirming profound myelin dysfunction in the internal capsule.

Taken together, the structural and quantitative impairment of myelin in the internal capsule disrupts the ISF drainage barrier between the caudate nucleus and thalamus—a key pathological event linking myelination defects to aberrant ISF distribution in SZ.

Discussion

In the present study, we utilized a chronic MK-801 administration model to simulate the core cognitive and SG deficits of SZ. Our findings reveal a novel pathological cascade: MK-801-induced myelin degradation in the internal capsule disrupts the compartmentalized drainage of brain ISF, leading to abnormal "reflux" between the caudate nucleus and the thalamus. This fluidic breakdown, in turn, triggers regional-specific metabolic dysregulation, particularly involving tryptophan and tyrosine pathways (Figure 6). These results provide a "fluidic dynamics" perspective on the neurochemical hypothesis of SZ.

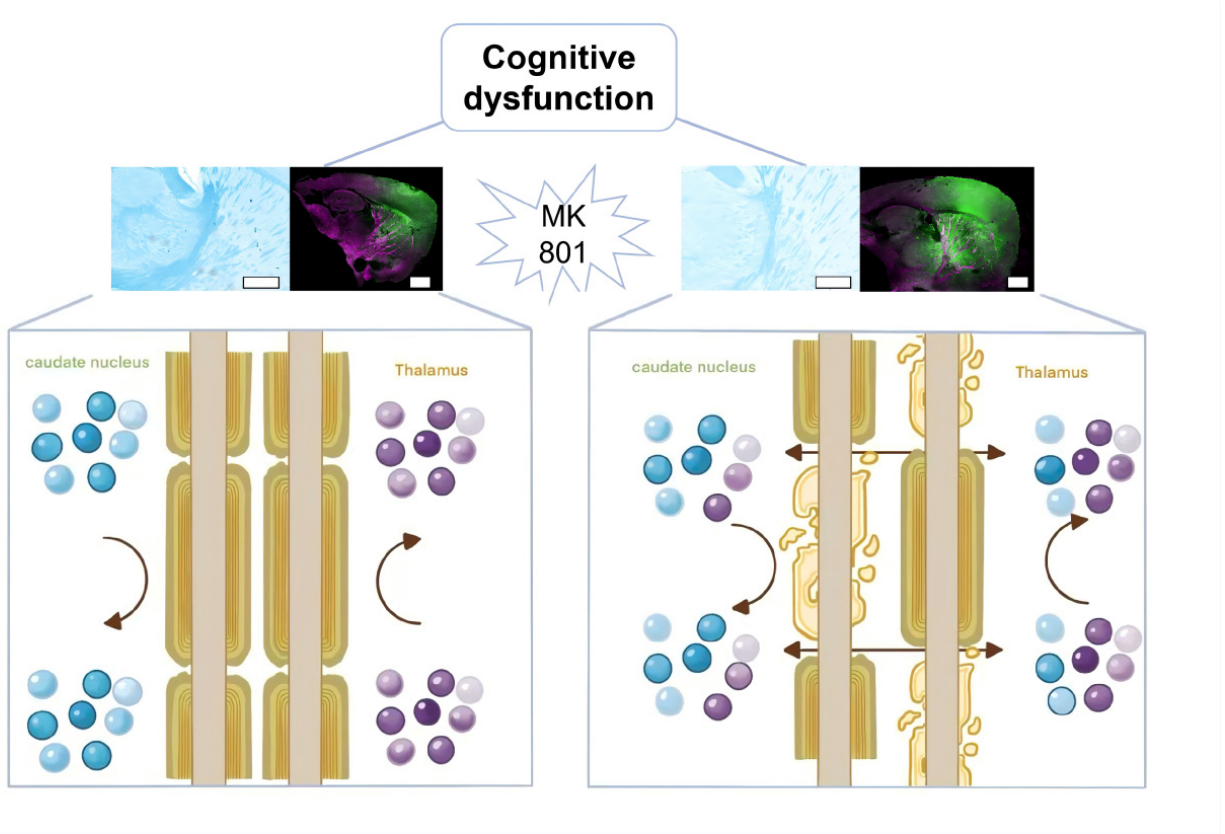

Figure 6. MK-801 induced cognitive dysfunction via refluxed interstitial fluid (ISF) and neurometabolites disturbance. Chronic MK-801 administration triggers myelin degradation in the internal capsule, which disrupts the compartmentalized drainage of brain ISF and causes abnormal "reflux" between the caudate nucleus and thalamus. This fluidic breakdown leads to regional-specific metabolic dysregulation, ultimately resulting in cognitive dysfunction. Upper panels show representative histological and immunofluorescent staining (scale bar = 4 mm) of the relevant brain regions in control and MK-801-treated animals; lower panels are schematic diagrams illustrating physiological ISF drainage with metabolite segregation (left) and pathological ISF reflux with metabolite disruption (right).

MK-801, as a potent non-competitive NMDA receptor antagonist, is widely recognized for inducing SZ-like symptoms in rodents, including cognitive impairment and SG deficits [26, 27]. Our behavioral data showed a significant reduction in the RI during the Novel Object Recognition test and a marked decrease in

PPI percentage. These results are consistent with previous reports that NMDA receptor hypofunction leads to disruptions in memory encoding and sensory filtering [28]. Notably, the absence of baseline startle or auditory response differences suggests that the observed deficits are centrally mediated rather than caused by peripheral sensory impairment [29, 30].

A key finding of this study is the severe structural impairment of the internal capsule in MK-801-treated mice [31–34]. The internal capsule, a major white matter tract, has recently been identified as a critical "barrier" structure that maintains the compartmentalized drainage of ISF between subcortical nuclei [13]. Our LFB staining and TEM analysis quantified this damage, showing significantly reduced myelin density and altered ultrastructure, including alternated myelin sheath thickness and G-ratio [35, 36].

The decreased G-ratio and increased thickness likely reflect pathological swelling or "loosening" of the myelin lamellae, a phenomenon often observed in the early stages of demyelinating insults [37]. Since the directional drainage of ISF relies on the physical constraints provided by dense, intact myelin sheaths, the observed structural breakdown directly explains the loss of compartmentalization [12]. This supports the hypothesis that SZ may fundamentally be a "white matter disease," where myelin defects lead to broader physiological failures [38, 39]. Recent high-impact clinical evidence further supports this structural barrier hypothesis; diffusion tensor imaging (DTI) has consistently identified increased impairment in the white matter of SZ patients [40, 41].

The breakdown of the myelin barrier facilitated an abnormal "reflux" of ISF from the caudate nucleus to the posterior thalamus. Under physiological conditions, ISF drainage is strictly partitioned to prevent the random mixing of neuroactive substances and metabolic byproducts [42–44]. Our results show that in the SZ model, this partitioning fails, potentially leading to "metabolic noise" or the cross-contamination of regional microenvironments. This 'fluidic' perspective is corroborated by emerging glymphatic research. Recent studies using DTI-ALPS imaging have demonstrated significant glymphatic clearance impairment in SZ patients, suggesting that a global failure in the brain's waste removal system contributes to the accumulation of neurotoxic metabolic byproducts [45, 46]. Our findings suggest that the myelin-based drainage barrier is a prerequisite for maintaining this glymphatic efficiency [47].

Our metabolomic analysis identified distinct pathway dysregulation in the caudate nucleus and thalamus. In the caudate nucleus, the significant enrichment of tryptophan metabolism is highly relevant to SZ pathology [48, 49]. Tryptophan is the precursor for the kynurenine pathway; its dysregulation can lead to the accumulation of kynurenic acid (KYNA), an endogenous NMDA receptor antagonist that further exacerbates cognitive dysfunction [50]. Simultaneously, the thalamic alterations in tyrosine metabolism—the rate-limiting precursor for dopamine synthesis—suggest that ISF reflux may disrupt the localized dopamine balance required for high-fidelity signal processing in the thalamocortical circuit [51, 52]. The observed ISF reflux may serve as a vehicle for the 'pathological spreading' of neuroactive metabolites. For instance, dysregulated kynurenine pathway intermediates—which are potent endogenous NMDA receptor modulators—could potentially drift from the striatum to the thalamus via refluxed ISF [53]. This 'metabolic cross-talk' likely exacerbates the baseline NMDA hypofunction, further destabilizing the Cortico-Striato-Thalamo-Cortical (CSTC) loop and driving cognitive deficits [54].

The interaction between the striatum (caudate nucleus) and the thalamus is a cornerstone of the CSTC loop, which regulates sensory filtering and cognitive control [55, 56]. What is more, the striatum is implicated in the regulation of sleep-wake cycles, which accounts for the occurrence of circadian rhythm disturbances in MK-801-induced SZ models, eventually impairing cognitive function [57, 58]. Our study suggests that the "fluidic" connection (ISF reflux) caused by myelin damage may disrupt the neurochemical integrity of this loop. Rather than a localized receptor deficit, the cognitive symptoms in SZ may stem from a global failure of the brain's "waste clearance" and "substance partitioning" systems [59, 60].

However, some limitations remain. While we established a correlation between ISF reflux and behavioral deficits, the temporal sequence of these events—whether myelin damage precedes or follows initial neurochemical shifts—requires further longitudinal study. Our data suggest a potential sequential

relationship between myelin degradation, ISF reflux, and metabolic disorders, but further mechanistic studies are required to confirm the exact causal cascade, as well as the direct link between ISF dysfunction and cognitive impairment. Future research should investigate whether pro-myelinating therapies can restore ISF drainage patterns and subsequently rescue cognitive function in SZ models.

Abbreviations

CLSM: confocal laser scanning microscope

CSTC: Cortico-Striato-Thalamo-Cortical

DTI: diffusion tensor imaging

i.p.: intraperitoneal injection

ISF: interstitial fluid

LFB: Luxol Fast Blue

NMDA: *N*-methyl-*D*-aspartate

OD: optical density

PLS-DA: partial least squares-discriminant analysis

PPI: pre-pulse inhibition

QC: quality control

RI: recognition index

SG: sensorimotor gating

SZ: schizophrenia

TEM: transmission electron microscopy

Supplementary materials

The supplementary table for this article is available at: https://www.explorationpub.com/uploads/Article/file/1006140_sup_1.pdf.

Declarations

Acknowledgments

We would like to express our gratitude to BGI Genomics (Shenzhen, China) for their professional assistance and technical support in high-resolution mass spectrometry and the untargeted metabolomics testing used in this study.

Author contributions

XM: Conceptualization, Methodology, Writing—original draft, Investigation. TG: Investigation, Writing—review & editing. SY: Software, Formal analysis, Data curation. HT: Investigation. SY: Software, Formal analysis, Data curation, Writing—review & editing. SS: Supervision, Funding acquisition. RL: Writing—original draft, Supervision, Funding acquisition, Visualization. All authors read and approved the submitted version.

Conflicts of interest

The authors declare that they have no conflicts of interest.

Ethical approval

The experimental protocols were reviewed and approved by the Institutional Animal Care and Use Committee of Peking University (LA2022325). All procedures followed the ethical guidelines for the care and use of laboratory animals.

Consent to participate

Not applicable.

Consent to publication

Not applicable.

Availability of data and materials

Any additional information that supports the findings reported in this study is available by contacting the corresponding author upon reasonable request.

Funding

Project supported by the Young Scientists Fund of the National Natural Science Foundation of China [Grant No.12401626]. The funder had no role in study design, data collection and analysis, decision to publish, or preparation of the manuscript.

Publisher's note

Open Exploration maintains a neutral stance on jurisdictional claims in published institutional affiliations and maps. All opinions expressed in this article are the personal views of the author(s) and do not represent the stance of the editorial team or the publisher.

References

1. He J, Zu Q, Wen C, Liu Q, You P, Li X, et al. Quetiapine Attenuates Schizophrenia-Like Behaviors and Demyelination in a MK-801-Induced Mouse Model of Schizophrenia. Front Psychiatry. 2020;11:843. [DOI] [PubMed] [PMC]
2. Marder SR, Umbricht D. Negative symptoms in schizophrenia: Newly emerging measurements, pathways, and treatments. Schizophr Res. 2023;258:71–7. [DOI] [PubMed]
3. Fond GB, Yon DK, Tran B, Mallet J, Urbach M, Leignier S, et al. Poverty and inequality in real-world schizophrenia: a national study. Front Public Health. 2023;11:1182441. [DOI] [PubMed] [PMC]
4. Solmi M, Seitidis G, Mavridis D, Correll CU, Dragioti E, Guimond S, et al. Incidence, prevalence, and global burden of schizophrenia—data, with critical appraisal, from the Global Burden of Disease (GBD) 2019. Mol Psychiatry. 2023;28:5319–27. [DOI] [PubMed]
5. Kadakia A, Catillon M, Fan Q, Williams GR, Marden JR, Anderson A, et al. The Economic Burden of Schizophrenia in the United States. J Clin Psychiatry. 2022;83:e83. [DOI] [PubMed]
6. Stępnicki P, Kondej M, Kaczor AA. Current Concepts and Treatments of Schizophrenia. Molecules. 2018;23:2087. [DOI] [PubMed] [PMC]
7. Faden J, Citrome L. Schizophrenia: One Name, Many Different Manifestations. Med Clin N Am. 2023; 107:61–72. [DOI] [PubMed]
8. Howes OD, Kapur S. The Dopamine Hypothesis of Schizophrenia: Version III--The Final Common Pathway. Schizophr Bull. 2009;35:549–62. [DOI] [PubMed] [PMC]
9. Onwordi EC, Whitehurst T, Mansur A, Statton B, Berry A, Quinlan M, et al. The relationship between synaptic density marker SV2A, glutamate and N-acetyl aspartate levels in healthy volunteers and schizophrenia: a multimodal PET and magnetic resonance spectroscopy brain imaging study. Transl Psychiatry. 2021;11:393. [DOI] [PubMed] [PMC]
10. Yang AC, Tsai SJ. New Targets for Schizophrenia Treatment beyond the Dopamine Hypothesis. Int J Mol Sci. 2017;18:1689. [DOI] [PubMed] [PMC]

11. Hung CC, Lin CH, Lane HY. Cystine/Glutamate Antiporter in Schizophrenia: From Molecular Mechanism to Novel Biomarker and Treatment. Int J Mol Sci. 2021;22:9718. [DOI] [PubMed] [PMC]
12. Wang R, Han H, Shi K, Alberts IL, Rominger A, Yang C, et al. The Alteration of Brain Interstitial Fluid Drainage with Myelination Development. Aging Dis. 2021;12:1729–40. [DOI] [PubMed] [PMC]
13. Wang A, Wang R, Cui D, Huang X, Yuan L, Liu H, et al. The Drainage of Interstitial Fluid in the Deep Brain is Controlled by the Integrity of Myelination. Aging Dis. 2019;10:937–48. [DOI] [PubMed] [PMC]
14. Falkai P, Raabe F, Bogerts B, Schneider-Axmann T, Malchow B, Tatsch L, et al. Association between altered hippocampal oligodendrocyte number and neuronal circuit structures in schizophrenia: a postmortem analysis. Eur Arch Psychiatry Clin Neurosci. 2019;270:413–24. [DOI] [PubMed]
15. Valdés-Tovar M, Rodríguez-Ramírez AM, Rodríguez-Cárdenas L, Sotelo-Ramírez CE, Camarena B, Sanabrais-Jiménez MA, et al. Insights into myelin dysfunction in schizophrenia and bipolar disorder. World J Psychiatry. 2022;12:264–85. [DOI] [PubMed] [PMC]
16. DeLisi LE. Current concepts in schizophrenia research: advancing progress towards understanding etiology and new treatments in year 2004—editorial comment. Curr Opin Psychiatry. 2005;18: 109–10. [DOI] [PubMed]
17. Richetto J, Meyer U. Epigenetic Modifications in Schizophrenia and Related Disorders: Molecular Scars of Environmental Exposures and Source of Phenotypic Variability. Biol Psychiatry. 2021;89:215–26. [DOI] [PubMed]
18. Bondi C, Matthews M, Moghaddam B. Glutamatergic animal models of schizophrenia. Curr Pharm Des. 2012;18:1593–604. [DOI] [PubMed]
19. Mao X, Han D, Guo W, Zhang W, Wang H, Zhang G, et al. Lateralized brunt of sleep deprivation on white matter injury in a rat model of Alzheimer's disease. GeroScience. 2023;46:2295–315. [DOI] [PubMed] [PMC]
20. Powell SB, Zhou X, Geyer MA. Prepulse inhibition and genetic mouse models of schizophrenia. Behav Brain Res. 2009;204:282–94. [DOI] [PubMed] [PMC]
21. Li B, Li C, Mao X, Gong X, Liu X, Han H, et al. Enhancing Cognitive Functions in Aged Rats Through Red Light Stimulation: A Focus on Hippocampal-Thalamic Interaction. Sens Imaging. 2025;27:e27. [DOI]
22. Engelke UF, van Outersterp RE, Merx J, van Geenen FA, van Rooij A, Berden G, et al. Untargeted metabolomics and infrared ion spectroscopy identify biomarkers for pyridoxine-dependent epilepsy. J Clin Investig. 2021;131:e131. [DOI] [PubMed] [PMC]
23. Klüver H, Barrera E. A method for the combined staining of cells and fibers in the nervous system. J Neuropathol Exp Neurol. 1953;12:400–3. [DOI] [PubMed]
24. Fan X, Mao X, Yu P, Han D, Chen C, Wang H, et al. Sleep disturbance impaired memory consolidation via lateralized disruption of metabolite in the thalamus and hippocampus: A cross-sectional proton magnetic resonance spectroscopy study. J Alzheimer's Dis. 2024;102:1057–73. [DOI] [PubMed]
25. Tang Y, Zhu H, Xiao L, Li R, Han H, Tang W, et al. Individual cerebellar metabolic connectome in patients with MTLE and NTLE associated with surgical prognosis. Eur J Nucl Med Mol Imaging. 2024; 51:3600–16. [DOI] [PubMed]
26. Benvenutti R, Gallas-Lopes M, Marcon M, Reschke CR, Herrmann AP, Piato A. Glutamate NMDA Receptor Antagonists with Relevance to Schizophrenia: A Review of Zebrafish Behavioral Studies. Curr Neuropharmacol. 2022;20:494–509. [DOI] [PubMed] [PMC]
27. Cadinu D, Grayson B, Podda G, Harte MK, Doostdar N, Neill JC. NMDA receptor antagonist rodent models for cognition in schizophrenia and identification of novel drug treatments, an update. Neuropharmacology. 2018;142:41–62. [DOI] [PubMed]
28. Carlsson ML, Carlsson A, Nilsson M. Schizophrenia: From Dopamine to Glutamate and Back. Curr Med Chem. 2004;11:267–77. [DOI] [PubMed]
29. Jafari Z, Kolb BE, Mohajerani MH. Prepulse inhibition of the acoustic startle reflex and P50 gating in aging and alzheimer's disease. Ageing Res Rev. 2020;59:101028. [DOI] [PubMed]

30. Castellano C, Cestari V, Ciamei A. NMDA Receptors and Learning and Memory Processes. Curr Drug Targets. 2001;2:273–83. [DOI] [PubMed]
31. Sun ZY, Ma DL, Gu LH, Chen X, Zhang L, Li L. DHF-7 Ameliorates Behavioral Disorders and White Matter Lesions by Regulating BDNF and Fyn in a Mouse Model of Schizophrenia Induced by Cuprizone and MK-801. Int J Neuropsychopharmacol. 2022;25:600–12. [DOI] [PubMed] [PMC]
32. Sırrı Akosman M, Türkmen R, Demirel HH. The protective effect of N-acetylcysteine against MK-801-induced neurodegeneration in mice. Mol Biol Rep. 2023;50:10287–99. [DOI] [PubMed]
33. Yu K, Zhou H, Chen Z, Lei Y, Wu J, Yuan Q, et al. Mechanism of cognitive impairment and white matter damage in the MK-801 mice model of schizophrenia treated with quetiapine. Behav Brain Res. 2024; 461:114838. [DOI] [PubMed]
34. Xiu Y, Kong XR, Zhang L, Qiu X, Chao FL, Peng C, et al. White Matter Injuries Induced by MK-801 in a Mouse Model of Schizophrenia Based on NMDA Antagonism. Anat Rec. 2014;297:1498–507. [DOI] [PubMed]
35. Guy J, Ellis EA, Kelley K, Hope GM. Spectra of G ratio, myelin sheath thickness, and axon and fiber diameter in the guinea pig optic nerve. J Comp Neurol. 2004;287:446–54. [DOI] [PubMed]
36. Gow A. Demystifying The Myelin *g* Ratio: Its Origin, Derivation and Interpretation. ASN Neuro. 2025; 17:2542166. [DOI] [PubMed] [PMC]
37. Sui YV, Bertisch H, Goff DC, Samsonov A, Lazar M. Quantitative magnetization transfer and g-ratio imaging of white matter myelin in early psychotic spectrum disorders. Mol Psychiatry. 2025;30: 2739–47. [DOI] [PubMed] [PMC]
38. Kochunov P, Hong LE. Neurodevelopmental and Neurodegenerative Models of Schizophrenia: White Matter at the Center Stage. Schizophr Bull. 2014;40:721–8. [DOI] [PubMed] [PMC]
39. Zovetti N, Bellani M, Chowdury A, Alessandrini F, Zoccatelli G, Perlini C, et al. Inefficient white matter activity in Schizophrenia evoked during intra and inter-hemispheric communication. Transl Psychiatry. 2022;12:449. [DOI] [PubMed] [PMC]
40. Gao J, Tang H, Wang Z, Li Y, Luo N, Song M, et al. Graph Neural Networks and Multimodal DTI Features for Schizophrenia Classification: Insights from Brain Network Analysis and Gene Expression. Neurosci Bull. 2025;41:933–50. [DOI] [PubMed] [PMC]
41. Carreira Figueiredo I, Borgan F, Pasternak O, Turkheimer FE, Howes OD. White-matter free-water diffusion MRI in schizophrenia: a systematic review and meta-analysis. Neuropsychopharmacology. 2022;47:1413–20. [DOI] [PubMed] [PMC]
42. Niedzwiecki MM, Samant P, Walker DI, Tran V, Jones DP, Prausnitz MR, et al. Human Suction Blister Fluid Composition Determined Using High-Resolution Metabolomics. Anal Chem. 2018;90:3786–92. [DOI] [PubMed] [PMC]
43. Dong Y, Xu T, Yuan L, Wang Y, Yu S, Wang Z, et al. Cerebrospinal fluid efflux through dynamic paracellular pores on venules as a missing piece of the brain drainage system. Exploration. 2023;4: 20230029. [DOI] [PubMed] [PMC]
44. Cheng Y, Liu J, Tian F, Tan H, Wang T, Lu J, et al. New Insight into the Mechanism of Neurochemical Imbalance in Multiple Sclerosis: Abnormal Transportation of Brain Extracellular Space. aging dis. 2024;17:452–65. [DOI] [PubMed] [PMC]
45. Chen H, Xiang H, Zhang M, Wen Y, Tang S, Tan S, et al. Antipsychotic-disease duration interaction on glymphatic function in first-episode schizophrenia: Evidence from DTI-ALPS. Schizophr Res. 2026; 289:79–88. [DOI] [PubMed]
46. Zhang X, Hatoum L, Ying J, Huang C. Assessing glymphatic-associated fluid dynamics in psychiatric disorders: evidence from neuroimaging—a review. Psychoradiology. 2025;5:kkaf031. [DOI] [PubMed] [PMC]
47. Lohela TJ, Lilius TO, Nedergaard M. The glymphatic system: implications for drugs for central nervous system diseases. Nat Rev Drug Discov. 2022;21:763–79. [DOI] [PubMed]

48. Chiappelli J, Postolache TT, Kochunov P, Rowland LM, Wijtenburg SA, Shukla DK, et al. Tryptophan Metabolism and White Matter Integrity in Schizophrenia. Neuropsychopharmacology. 2016;41: 2587–95. [DOI] [PubMed] [PMC]
49. Cervenka I, Agudelo LZ, Ruas JL. Kynurenines: Tryptophan's metabolites in exercise, inflammation, and mental health. Science. 2017;357:e357. [DOI]
50. Schwarcz R, Bruno JP, Muchowski PJ, Wu HQ. Kynurenines in the mammalian brain: when physiology meets pathology. Nat Rev Neurosci. 2012;13:465–77. [DOI] [PubMed] [PMC]
51. Sánchez-González MA, García-Cabezas MA, Rico B, Cavada C. The primate thalamus is a key target for brain dopamine. J Neurosci. 2005;25:6076–83. [DOI] [PubMed]
52. Szigetvari PD, Patil S, Birkeland E, Kleppe R, Haavik J. The effects of phenylalanine and tyrosine levels on dopamine production in rat PC12 cells. Implications for treatment of phenylketonuria, tyrosinemia type 1 and comorbid neurodevelopmental disorders. Neurochem Int. 2023;171:105629. [DOI] [PubMed]
53. Sapienza J, Spangaro M, Guillemin GJ, Comai S, Bosia M. Importance of the dysregulation of the kynurenine pathway on cognition in schizophrenia: a systematic review of clinical studies. Eur Arch Psychiatry Clin Neurosci. 2022;273:1317–28. [DOI] [PubMed]
54. Collin G, Turk E, van den Heuvel MP. Connectomics in Schizophrenia: From Early Pioneers to Recent Brain Network Findings. Biol Psychiatry: Cogn Neurosci Neuroimaging. 2016;1:199–208. [DOI] [PubMed]
55. Byne W, Hazlett EA, Buchsbaum MS, Kemether E. The thalamus and schizophrenia: current status of research. Acta Neuropathol. 2008;117:347–68. [DOI] [PubMed]
56. Peters SK, Dunlop K, Downar J. Cortico-Striatal-Thalamic Loop Circuits of the Salience Network: A Central Pathway in Psychiatric Disease and Treatment. Front Syst Neurosci. 2016;10:104. [DOI] [PubMed] [PMC]
57. Wang Q, Zhu D, Ping S, Li C, Pang K, Zhu S, et al. Melatonin recovers sleep phase delayed by MK-801 through the melatonin MT_2 receptor- Ca^{2+}-CaMKII-CREB pathway in the ventrolateral preoptic nucleus. J Pineal Res. 2020;69:e12674. [DOI] [PubMed]
58. Dong H, Chen ZK, Guo H, Yuan XS, Liu CW, Qu WM, et al. Striatal neurons expressing dopamine D1 receptor promote wakefulness in mice. Curr Biol. 2022;32:600–13.e4. [DOI] [PubMed]
59. Kirino E, Tanaka S, Fukuta M, Inami R, Inoue R, Aoki S. Functional Connectivity of the Caudate in Schizophrenia Evaluated with Simultaneous Resting-State Functional MRI and Electroencephalography Recordings. Neuropsychobiology. 2018;77:165–75. [DOI] [PubMed]
60. Aggleton JP, O'Mara SM. The anterior thalamic nuclei: core components of a tripartite episodic memory system. Nat Rev Neurosci. 2022;23:505–16. [DOI] [PubMed]